New Journal of Physics
The open access journal at the forefront of physics

Deutsche Physikalische Gesellschaft DPG IOP Institute of Physics

PAPER • OPEN ACCESS

Mechanical and electrical properties of a nano-gap or how to play the nano-accordion

To cite this article: Simon Hettler and Raul Arenal 2026 *New J. Phys.* **28** 033504

View the article online for updates and enhancements.

You may also like

- (Invited) Probing the Structure and Dynamic Behaviors of Heterogeneous Functional Materials with the Atomic Resolution in Real-Time
Xiaoqing Pan

- Correlated and in-situ electrical transmission electron microscopy studies and related membrane-chip fabrication
Maria Spies, Zahra Sadre Momtaz, Jonas Lähnemann et al.

- In-situ transmission electron microscopy for probing the dynamic processes in materials
Yuchen Zhu, Haofei Zhao, Yang He et al.

This content was downloaded from IP address 129.13.194.163 on 22/04/2026 at 09:38

New Journal of Physics
The open access journal at the forefront of physics

Published in partnership with: Deutsche Physikalische Gesellschaft and the Institute of Physics

OPEN ACCESS

RECEIVED
19 November 2025

REVISED
22 February 2026

ACCEPTED FOR PUBLICATION
6 March 2026

PUBLISHED
16 March 2026

Original content from this work may be used under the terms of the Creative Commons Attribution 4.0 licence.

Any further distribution of this work must maintain attribution to the author(s) and the title of the work, journal citation and DOI.

PAPER

Mechanical and electrical properties of a nano-gap or how to play the nano-accordion

Simon Hettler[1,2,3,*] and Raul Arenal[2,3,4]

1 Laboratory for Electron Microscopy, Karlsruhe Institute of Technology, Karsruhe, Germany
2 Instituto de Nanociencia y Materiales de Aragón (INMA), CSIC-Universidad de Zaragoza, Zaragoza, Spain
3 Laboratorio de Microscopías Avanzadas (LMA), Universidad de Zaragoza, Zaragoza, Spain
4 ARAID Foundation, Zaragoza, Spain
* Author to whom any correspondence should be addressed.

E-mail: simon.hettler@kit.edu

Keywords: *in-situ* transmission electron microscopy, nano-gap, grain boundary, mechanical bending, intrinsic voltage

Supplementary material for this article is available online

Abstract

In-situ transmission electron microscopy (TEM) has become an important technique to study dynamic processes at highest spatial resolution and one branch is the investigation of phenomena related with electrical currents. Here, we present experimental results obtained from a peculiar *in-situ* TEM device, which was prepared with the aim to analyze the relationship between (thermo) electric properties and specific crystal orientations of a misfit layered compound. The formation of a nano-sized gap at a grain boundary facilitated a precisely controllable mechanical bending of the device by application of differential heating currents. The devices' electrical properties were found to be substantially influenced by the gap, leading to a high intrinsic voltage. This voltage additionally depends on the vacuum environment and on the history of applied heating currents with internal field strengths of up to 37 kV m^{-1}. These findings are largely attributed to the presence of adsorbed molecules within the gap region. The electrical *in-situ* TEM studies of this work illustrate that interior surfaces can strongly influence electrical properties even under high vacuum conditions.

1. Introduction

Electrical conduction in matter is mainly governed by the materials' band structure and electron scattering processes in the material. In pristine single-crystalline bulk specimens and at finite temperatures and bias, electron-phonon interaction is the limiting factor for the conductivity. In real samples, scattering from defects in the material constitutes an additional contribution. The microstructure, including interfaces, surfaces, grain boundaries and point defects, can therefore significantly alter the electrical conductivity of real materials in comparison to defect-free single crystals. The relationship between microstructure and electrical conductivity has been subject of investigation for a long time [1, 2] and research is continuing until today, with the motivation to improve the conductivity of electrical interconnects or the performance of thermoelectric materials [3–6].

Due to the continuing miniaturization of electronic devices, microscopic approaches to analyze the impact of individual defects on the electrical conductivities have been followed in the past decades [7, 8]. Specifically, *in-situ* transmission electron microscopy (TEM) has received interest due to its high spatial resolution [9–12]. Only recently, the possibility of performing *in-situ* TEM thermoelectric characterizations has been demonstrated [13]. Several misfit-layered compound (MLC) families are promising materials for thermoelectric applications [14]. In bulk MLC materials, both grain boundaries and pore density are expected to have a strong impact on their performance.

© 2026 The Author(s). Published by IOP Publishing Ltd on behalf of the Institute of Physics and Deutsche Physikalische Gesellschaft

This work is part of an experiment series, where different *in-situ* TEM specimens of a strontium-doped variant of the calcium cobaltite (CCO) MLC family ($Ca_{2.93}Sr_{0.07}Co_4O_9$) [15] have been prepared with the aim of elucidating the impact of grain boundaries and crystallographic directions on the (thermo)electric properties. Here, we present experimental results obtained from one peculiar *in-situ* TEM device of this series, which exhibited a nano-sized gap and will be named nano-accordion throughout the manuscript. The name is motivated by the controlled mechanical movement of the device induced by an applied differential heating current, which resembles the folding and unfolding of an accordions' bellows. The gap also has a strong impact on the electrical characteristics, manifesting itself as a large intrinsic voltage offset, which is attributed to adsorbed molecules present in the gap region.

2. Materials and methods

2.1. *In-situ* TEM

In-situ TEM investigations were carried out using two aberration-corrected (one probe-, the other image-corrected) Titan microscopes (Thermo Fisher Scientific) operated at 300 keV. Both microscopes were used for bright-field (BF) and dark-field (DF)-TEM imaging as well as for selected-area electron diffraction (SAED). High-angle annular dark field (HAADF) scanning (S)TEM was performed in the probe-corrected microscope and high-resolution (HR)TEM imaging was performed in the image-corrected microscope. SAED patterns were simulated using the ReciPro software [16].

A DENSolutions Wildfire specimen holder with a custom chip designed for *in-situ* thermoelectrical characterizations [13] was used to conduct the *in-situ* TEM experiments. Fabrication of the chip is described elsewhere [13]. The chip contains a silicon nitride membrane with a thickness of 1 μm in its center, on which two contact pads and a differential heating element have been structured by lithography. A scanning electron microscopy (SEM) image of the membrane area of the chip is shown in figure 1(a). The application of a heating current to the differential heating element results in the generation of a temperature gradient along a specimen that is placed between the two contact pads. A long hole of more than 50 μm length is milled in the silicon nitride membrane between the two pads, which acts as thermal insulation barrier and thus ensures the generation of a large temperature gradient [13]. The hole is (partially) seen in the SEM images of the final device shown in figures 1(c) and (d). The temperature increase of the heating element $\Delta T_{\mathrm{H,est}}$ can be estimated from the two-point measurement of the heater resistance as described in the supplementary figure S1. Despite being only an estimation for the actual temperature of the investigated area of the device, it is instructive to plot the measured characteristics over the temperature instead of the applied heating current I_{H}.

2.2. Specimen preparation

The *in-situ* TEM specimen was prepared using a Helios 650 dual-beam instrument (Thermo Fisher Scientific) combining SEM with a Ga^+ focused ion beam (FIB). In a first step, a conventional TEM lamella was prepared from a strontium-doped calcium cobaltite (CCO: $Ca_{2.93}Sr_{0.07}Co_4O_9$) MLC. The preparation of the bulk CCO material is described in [15] and starts with attrition milling of $SrCO_3$, $CaCO_3$ and CoO, followed by calcination at 850 °C during 1 h, uniaxial pressing under 250 MPa and hot-uniaxial pressing at 900 °C and 51 MPa for 1 h. The CCO material consists of the two subsystems CoO_2 and $Ca_{2-x}Sr_xCoO_3$, which are stacked alternately along the *c* axis of the incommensurate crystal structure, which is sketched in the inset of figure 1(b). Figure 1(b) also shows an SEM image of the CCO material, which exhibits numerous sheets in vertical direction of the image. The out-of-plane direction of the sheets (horizontal in the image) roughly corresponds to the *c* axis of the CCO material. The TEM lamella was prepared with the *c* axis of the CCO material coinciding with the long axis of the lamella, which is seen from the deposited stripe of Pt in figure 1(b), which served as protection layer for the lamella. The lamella was then transferred to a TEM grid using a standard lift-out method. The lower side of the lamella was polished to guarantee a good contact with the *in-situ* chip in the next step. In the central part, several hundreds of nanometers of the lamella were removed on the lower side, resulting in a bridge-like shape. This bridge-like shape facilitates the later thinning of the lamella on the *in-situ* chip and is revealed in the inset image in figure 1(c). The inset image shows the top-view of the lamella on the grid.

To transfer the lamella to the *in-situ* chip, both the chip and the grid (lying flat on the surface) were mounted on separate stubs in the dual-beam instrument. First, a long hole was milled between the contact pads of the *in-situ* chip by FIB. The lamella was then lifted out from the TEM grid, deposited on the chip, and fixed by FIB-induced deposition of Pt. For thinning, the chip was mounted on a stub with a surface with a vertical inclination of 45°. Thinning of the lamella was performed at a stage tilt

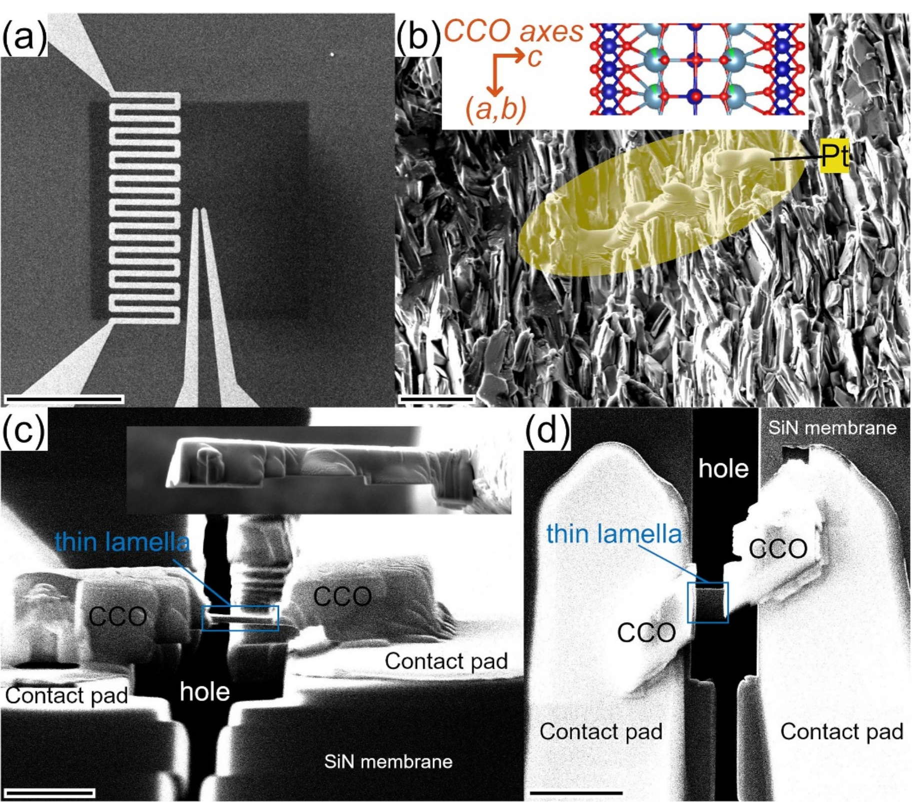

Figure 1. Preparation of the nano-accordion. (a) SEM image of the membrane area with the differential heating element and the contact pads of the *in-situ* chip, see (d) for a zoomed-in view of the pads. (b) SEM image of the CCO material reveals its sheet-like structure, the predominant *c* axis direction of the material has been indicated. A sketch of the MLC structure with Co (dark blue), Ca/Sr (light blue/green) and O (red) atoms has been added. The deposited Pt, highlighted in yellow, indicates the place from where the lamella was taken and its orientation with respect to the CCO sheets. Stage tilt is 52°. (c) SEM image of the thinned device on the *in-situ* chip with an incident angle of the electron beam of 5° with respect to the surface of the chip. The two Pt contact pads, the thick ('CCO') and thin parts of the lamella as well as the long hole in the SiN membrane are visible. The inset shows the bridge-shaped form of the lamella after transfer to a Cu TEM grid. (d) Top view of the final *in-situ* device. Scale bars are (a) 200 μm, (b) 10 μm, (c) 2 μm, width of inset SEM image is 15 μm and (d) 5 μm.

of 12°, resulting in a FIB incident angle on the surface of the chip of 5° (figure 1(c)) due to the angle of 52° between FIB and electron beam. After thinning, the Pt protection cover was removed from the thin part of the device by FIB milling, leaving the thinned part with an approximately quadratic shape with a side length of 1.6 μm and a thickness of 120 nm (figure 1(c)). FIB operation voltage was 30 kV for all steps and final thinning current was 24 pA.

2.3. Electrical characterization

Two Keithley Instruments (Tektronix) devices were used for electrical characterization of the specimen (2450 SourceMeter) and simultaneous application of a heating current I_H to the differential heating element on the chip (2611A System Source Meter). The heating current was set manually, and the I–V characterization was performed with the Keithley Kickstart software.

3. Results and discussion

The CCO device was prepared with the aim of studying its thermoelectric properties, but the electrical measurements showed unexpected characteristics. A detailed TEM analysis revealed that a nano-gap formed in the device, which is described first in section 3.1. The mechanical properties of the device are described in the following section 3.2 before the electrical characterization is presented and discussed in section 3.3. Finally, the device characterization after the formation of a fully penetrating gap is presented in section 3.4.

3.1. Formation of a nano-gap at a grain boundary

Figure 2(a) shows a HAADF-STEM image of the thin part of the device at a stage tilt of 11.5°. At this tilt, the image reveals a dark vertical line, which corresponds to a nano-sized gap separating the left from the right sections of the lamella. The inset image shows that the gap extends over approximately half of

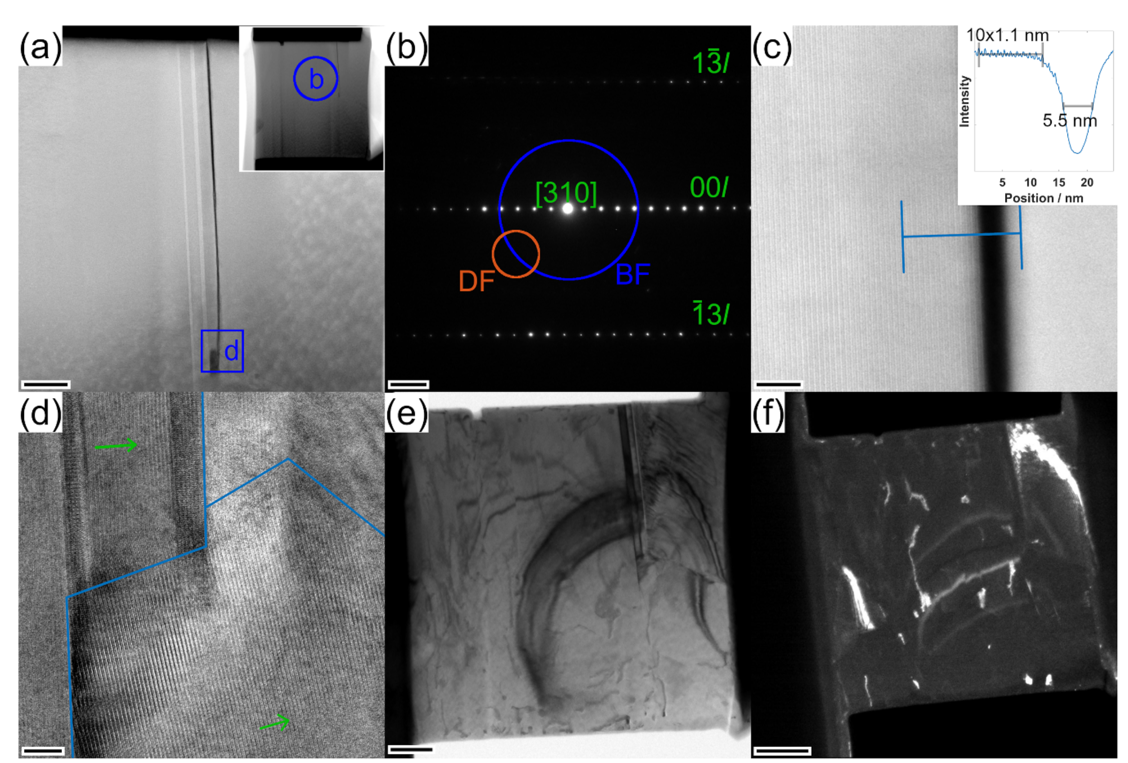

Figure 2. (a) HAADF-STEM image of the nano-accordion at a stage tilt of 11.5° revealing the presence of a gap in the device. The inset STEM image shows the entire region of the thin lamella. The selected area for the SAED pattern shown in (b) and the acquisition position of the HRTEM image shown in (d) are indicated. (b) SAED pattern taken from the area marked in (a) revealing the horizontal orientation of the *c* axis of the material in the left part of the lamella. The sets of [00*l*] and [13*l*] reflections are named and the placement position of the objective aperture for acquisition of the BF and DF-TEM images shown in (e) and (f) is indicated. (c) HRSTEM image of the central gap region revealing the stack along the *c*-axis on its left side. A line profile taken from the marked area is shown in the inset revealing a stack periodicity of 1.1 nm and a gap width of approximately 5.5 nm. (d) HRTEM image of the end of the gap with grain boundary positions (blue lines) and the direction of the respective *c*-axis orientation (green arrows) marked. (e) BF- and (f) DF-TEM images of the thin part of the lamella, description see text. Scale bars are (a) 100 nm, inset image width is 2 μm, (b) 2 nm^{-1}. (c) 9 nm, (d) 10 nm, (e) 200 nm and (f) 300 nm.

the height of the lamella. An SAED pattern taken from the left side of the gap (figure 2(b)) shows that in this region, the *c* axis of the CCO material agrees with the horizontal direction. The orientation of the CCO crystal is close to the [310] orientation of the $Ca_{2-x}Sr_xCoO_3$ subsystem as both sets of [00*l*] and [13*l*] reflections can be identified in the SAED pattern (figure 2(b)). In contrast, the electron beam direction does not agree with a higher-order crystal direction of the CCO material in the right part as revealed by a corresponding SAED pattern, shown in the supplementary figure S2.

The gap thus formed at a grain boundary of the material, which is also seen from HR STEM and TEM images taken from the gap region (figures 2(c) and (d), respectively). The HRSTEM image shows the stack periodicity on the left side of the gap. A line scan across the border allows to measure a periodicity of 1.1 nm (inset image in figure 2(c), which agrees with the reference value of 1.08 nm of the CCO material [17]. The HAADF-STEM image also shows that the left part of the lamella shows a bright line directly at the gap boundary indicating that the CCO material terminates with a layer of the CoO_2 subsystem, which shows stronger HAADF signal as the $Ca_{2-x}Sr_xCoO_3$ subsystem [18]. The line scan additionally reveals a gap width at this position of approximately 5.5 nm. The HRTEM image shown in figure 2(d) was acquired from the lower end of the gap and reveals that the gap originates at a triple grain boundary. Three grains are visible in the image and their borders have been marked by blue lines. The grain on the upper left side shows a horizontal *c*-axis orientation, indicated by a green arrow in figure 2(d), which is in agreement with the SAED pattern and the HRSTEM image in figure 2(b) and (c). In the lower grain, the stack periodicity is visible, but with a rotation compared to the previous grain. Finally, on the upper right side, no lattice fringes can be detected. At this position, the gap is not penetrating through the entire thickness of the lamella, but the partial gap is visible from the area with bright contrast forming along the grain boundary of the upper left grain.

Figures 2(e) and (f) show a BF-TEM and DF-TEM image of the lamella region with the respective placement of the objective apertures indicated in figure 2(b). In the BF-TEM image, dark areas correspond to regions, where an increased number of electrons undergo diffraction or scattering events to

higher angles than given by the objective aperture radius. As the lamella is made of a single material and exhibits a homogeneous thickness, the visible features correspond to diffraction contrast. A dark bend stripe can be seen in the image that originates in the lower part of the lamella and ends at the gap, indicating that in this area, the crystal exhibits a higher-order orientation with respect to the electron beam. At the same time, it indicates that the lamella is strongly bend as a relaxed grain with similar orientation throughout would exhibit a homogeneous contrast. The same observation can be made from the DF-TEM image shown in figure 2(f). The objective aperture was placed in a region where no major reflections of the [310] orientation is located (see orange circle in figure 2(b). Several small bright areas are visible in figure 2(f) that are caused by inclusions with different crystal orientation. In addition, a bright stripe is visible in the upper right grain, which indicates that also the right grain is strongly bend. Three thin white lines can be seen in the left grain, that are assumed to correspond to an additional minor reflection, possibly the [020] reflection of the $Ca_{2-x}Sr_xCoO_3$ subsystem.

This analysis of the nano-accordion reveals that there is a gap in the device and that the material is considerably bend. The formation of the gap could be attributed to two effects: Firstly, pores are frequently encountered in the CCO material and the gap could have corresponded to an elongated pore. Also, the layered structure of the MLC introduces internal stress, which can additionally facilitate the gap formation. Secondly, another plausible explanation is the opening of the gap at the grain boundary due to mechanical stress. On the one hand, the high-pressure fabrication process introduces considerable stress in the bulk material. The opening of the gap could be caused by a release of that stress. On the other hand, the lamella is subjected to possible mechanical stress on the device induced by the SiN membrane after cutting of the hole.

3.2. Thermally induced controlled bending of the specimen

In this section, the mechanical deformation of the device in response to the heating current I_H applied on the differential heating element is analyzed. For this analysis, the evolution of the device during the application of increasing I_H up to a maximum of 5 mA was followed by different TEM imaging and diffraction techniques. Figures 3(a)–(c) shows three BF-TEM images acquired at $I_H = 0$, 3 and 5 mA. The whole series of BF-TEM images is given in supplementary video S1. In the initial, unheated state (figure 3(a)), the dark broad bending contour corresponds to the [310] crystal orientation, as discussed previously for figure 2(e). With increasing applied heating current, the device starts to bend and the bending contour moves towards the left border of the lamella. From the gap region, additional bending contours appear, which can be linked to another minor zone-axis (figure 3(b)). At maximum I_H, this additional contours have similarly traveled towards the left border of the lamella. A movement of the contours in the opposite direction and with reduced speed is visible in the two grains located at the right border of the lamella, suggesting a reduced strength of the bending in that region. A difference is also seen between the top part, which includes the gap, and the bottom part, where the material is not separated by a gap. The movement of the contours is enhanced in the top part due to the presence of the gap.

The BF-TEM images also allow to measure the distance between the edges of the thick portion of the lamella as indicated by the blue line in figure 3(b). The measured width is plotted over the estimated heater temperature $\Delta T_{H,est}$ in figure 3(d) and reveals a close-to-linear decrease with the temperature. The width decreases by 22 nm when compared to the unheated state. The observed bending and the decreasing width are caused by a thermal expansion of the heated area of the *in-situ* chip. The small deviations from the linear decrease with temperature can be explained by an inhomogeneous temperature distribution within the *in-situ* chip.

In addition to BF-TEM imaging, the device was studied by DF-TEM imaging with similar conditions as in figure 2(f) and the corresponding images can be seen in supplementary video S2. The video shows a similar movement of the bending contours, confirming the considerable bending induced by the applied heating current I_H. Supplementary video S3 shows the evolution of the HAADF-STEM contrast in dependence of I_H. The HAADF-STEM image of the series acquired at $I_H = 5$ mA is displayed in figure 3(e). The image shows the gap-region of the device and instead of the dark line corresponding to the gap, a bright line with increasing width toward the upper border can be seen. This bright line is explained by the overlap between the right and left part of the lamella caused by the bending of both sides toward each other. Supplementary video S3 also reveals the change in channeling contrast due to bending and the related loss of parallelity of the electron beam with the *a-b* plane of the crystal close to the gap.

The SAED patterns for increasing I_H up to 5 mA can be seen in supplementary video S4 and figure 3(f) shows the SAED pattern at the maximum current of 5 mA. The pattern reveals that at this current, the electron beam current direction does not agree with a crystal plane of the CCO material.

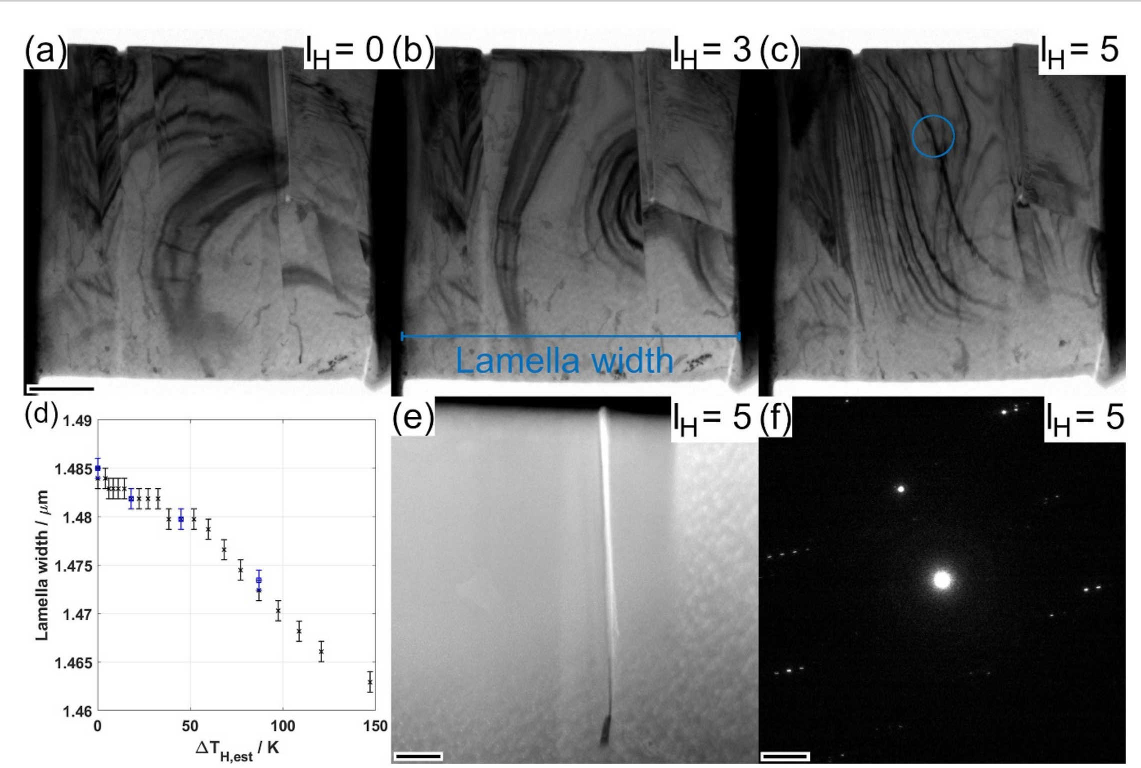

Figure 3. (a)–(c) BF-TEM images of the thin part of the device for different applied I_H of (a) 0 mA, (b) 3 mA and (c) 5 mA. The movement of the bending contours due to temperature-induced bending is clearly visible. (d) Plot of the measured width of the lamella as indicated by the blue line in (b) over $\Delta T_{H,est}$. The close-to-linear decreasing width due to thermal expansion and bending is clearly visible. Black crosses correspond to the rise of the current and blue boxes to the descent. Error bars correspond to the pixel size. (e) HAADF-STEM image of the device with $I_H = 5$ mA. The two parts of the lamella overlap in the upper part due to temperature-induced bending, which leads to the increased contrast in the overlapping region. (f) SAED pattern acquired from the area marked by a blue circle in (c) for $I_H = 5$ mA. Due to bending, the electron-beam direction is now far from the initial proximity to the [310] orientation. Scale bars are (a)–(c) 300 nm. (e) 100 nm and (f) 3 nm^{-1}.

The video reveals a smooth evolution of the SAED pattern. The experimental SAED patterns were compared qualitatively with simulated patterns considering only the $Ca_{2-x}Sr_xCoO_3$ subsystem of the CCO material (see supplementary figure S3). The comparison reveals that the orientation of the crystal with respect to the electron beam changes by approximately 8° between the unheated state and $I_H = 5$ mA.

The presented analysis clearly shows that an applied heating current allows to control the mechanical state of the device. This control is highly reproducible, a repeated applied heating current results in the identical mechanical state of the device as shown by the comparison of TEM images and SAED patterns for the same I_H at different points of time (see supplementary figure S4). The controlled movement of the device resembles the movement of the bellows during the operation of an accordion (musical instrument) and for that reason, the device was named nano-accordion.

3.3. Electrical characterization of the nano-gap

The employed *in-situ* chip allows to study the electrical characteristics of the device in dependence of the applied differential heating current I_H. Figure 4(a) shows three *I*–*V* curves obtained 1) at $I_H = 0$ mA shortly after insertion of the device in the microscope (solid blue line), 2) at $I_H = 5$ mA (solid red line) and 3) again in the unheated state after turning of the heating current (blue dashed line). The measured current is considerably increased in the heated case, which can be attributed to the semiconducting nature of the CCO material, whose conductivity increases with the temperature. The current has a non-linear dependency on the applied voltage, which is again explained by the semiconductivity of the material in combination with the considerable current densities ($>1.5\cdot10^3$ A cm^{-2}) at ±0.5 V and an expected Joule heating of the device.

The chip was designed such that an applied I_H leads to a temperature gradient along the device, which permits the study of the thermoelectric properties of the material [13]. To measure that induced voltage, the voltage at zero current is determined in dependence of the applied heating current. Three black squares are added to the inset in figure 4(a), which indicate the origin (left square) and the voltage offset for the red and blue solid curves (other squares). It is seen that even at no applied heating current,

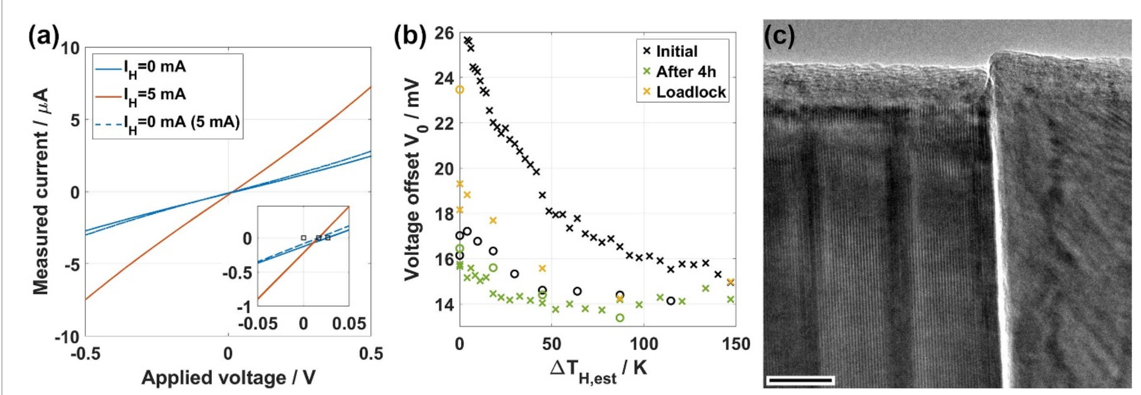

Figure 4. (a) Comparison of three I–V curves for $I_H = 0$ mA (blue solid line), $I_H = 5$ mA (red line) and again at 0 mA after having heated with 5 mA (blue dashed line). The inset shows the curves at low voltages and the black squares mark the origin and the voltages where blue and red curves pass zero measured current. (b) Plot of the voltage offset (as marked by black squares in the inset in (a)) for three different conditions of the device: Directly after insertion in the microscope (black crosses and circles), after 4 h in the microscope (green) and after retraction to the loadlock (yellow). (c) TEM image of the gap region directly after insertion showing a bright contrast in the gap region. Scale bar is 20 nm.

a strong voltage offset of 25 mV is measured, being too high to be a measurement error, which is typically well below 0.1 mV. The voltage offset is decreased for $I_H = 5$ mA and, more interestingly, the second I–V curve taken at 0 mA after heating, does not agree with the initial measurement.

Figure 4(a) shows only three curves of a measurement series for varying I_H. For each I–V curve, the voltage offset was determined and is plotted in black crosses and circles over $\Delta T_{H,est}$ in figure 4(b). The crosses correspond to the rise and the circles to the descent of the current and the difference is clearly seen. The same measurement series was repeated after 4 h of the device in the microscope (green crosses and circles), which does not show a significant difference between rise and descent and which agrees well with the descent of the initial measurement series. These observations suggest that the device undergoes a structural change during the first heating and remains in that state even if a current is applied again. In addition, figure 4(b) shows yellow crosses and circles, which correspond to a third measurement series, conducted after retracting the specimen holder to the loadlock position. For this measurement series, the voltage offset at $\Delta T_{H,est} = 0$ K after heating up is found to be higher than before, suggesting that the device underwent the initial process in reverse direction.

It is instructive to compare the measured I–V curves and voltage offsets with the measurements conducted on similar devices without gap [13]. The measured voltage offset in gap-free devices at $I_H = 0$ mA was in the range of 10 μV, thus being three orders of magnitude smaller than the offset measured for the nano-accordion. The thermo-voltage induced by the differential heating device followed a smooth, approximately quadratic evolution reaching maximum values of below 7 mV independent on the history of applied currents. This again strongly differs from the nano-accordion, which does not exhibit a well-defined dependency on $\Delta T_{H,est}$ and exhibits also considerably more noise. This comparison allows the conclusion, that, although the induced thermo-voltage plays a role in the measured characteristics of the nano-accordion, it is clearly not the dominant contribution.

These considerations suggest that the electrical characteristics of the device cannot be explained solely by the (thermo)electric properties of the material but are related to the nano-gap, absent in all other studied devices. The observed unexpected electrical characteristics may be attributed to molecules in the gap region. Water and hydrocarbon molecules are commonly adsorbed on specimens under the high-vacuum conditions typical for TEM and can be assumed to be present on the inner surfaces of the gap region as well. As hydrocarbon molecules are nonpolar, it is difficult to imagine how these can generate an intrinsic voltage. Therefore, it is reasonable to assume that (polar) water molecules will have the largest impact on the electrical properties of the nano-accordion and cause the large voltage offset observed in the unheated state. Indeed, water molecules are known to have a significant impact on the work function of a material if chemisorbed on the surface and a monolayer of perfectly aligned molecules corresponds to a voltage step of 4 V [19, 20]. Assuming that the gap is the sole cause for the voltage offset, the measured voltage offsets in the unheated state can be used to estimate the field strength within the gap region. With gap dimensions of $5 \times 120 \times 700$ nm^3, the field strength calculates to initially 1.5 kV m^{-1} and decreases to 0.95 kV m^{-1} after 4 h. These values can be seen as lower estimate as the gap width varies locally and extends only over half of the lamella. The decrease of the voltage offset after heating under high vacuum conditions is linked to the desorption of a considerable

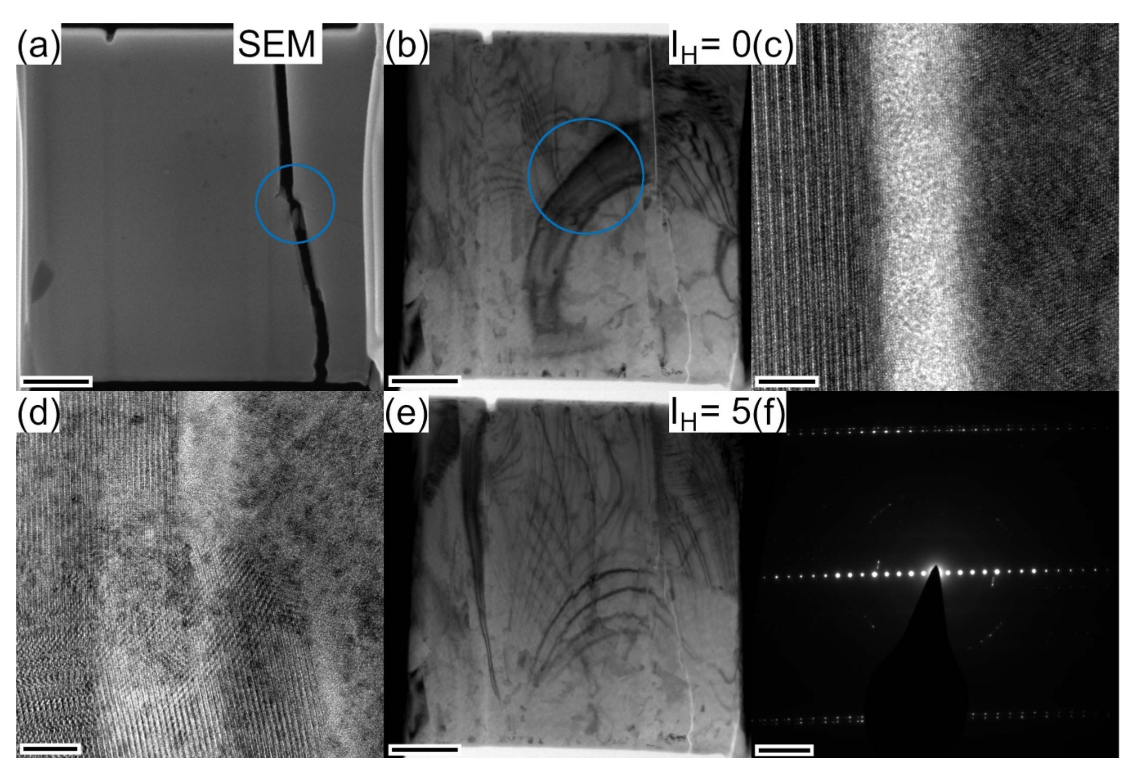

Figure 5. (a) SEM image of the device with full gap. The circle indicates the position with minimum distance. (b) BF-TEM images of the device with fully broken gap, circle indicates position for SAED pattern acquisition. (c) HRTEM image of the upper gap revealing amorphous material in the gap region. (d) HRTEM image of the triple-phase region showing that in this area, the gap only exhibits minimum width. (e) BF-TEM image of the device at an applied heating current of $I_{\mathrm{H}} = 5$ mA. (f) SAED pattern of the unheated device. Scale bars are (a), (b), (e) 300 nm, (c) 5 nm, (d) 10 nm, (f) 4 nm^{-1}.

portion of the molecules due to the increasing temperature and facilitated by the mechanical movement of the device that causes the exposure of the interior surfaces of the gap and thus favors the desorption. In contrast, the retraction to the loadlock of the microscope, an area with worse vacuum conditions, leads to the re-adsorption of (water) molecules and thus to an increase of the observed voltage offset. The decrease/increase of the voltage offset (figure 4(b)) exhibits a strong slope for $\Delta T_{\mathrm{H,est}} < 50$ K, which is smaller for higher $\Delta T_{\mathrm{H,est}}$. This suggests that the initial decrease is mainly caused by the mechanical movement and that temperature-induced effects only play a significant role for higher $\Delta T_{\mathrm{H,est}}$.

Figure 4(c) shows a HRTEM image of the gap region shortly after insertion in the microscope. The image was acquired in slight overfocus conditions and the gap region appears with bright contrast compared to the vacuum region. Under overfocus conditions, atoms (positive potential) appear bright, [21] indicating that indeed, material and/or positive charges are present in the gap region.

3.4. Characterization after formation of a gap along the entire device

After the conducted measurements presented in the preceding sections, the nano-accordion was mounted in the dual-beam machine with the aim to further thin the device and study the impact on the electrical characteristics. Figure 5(a) shows an SEM image of the device after mounting, which reveals that the gap opened across the entire lamella. The image reveals a gap width of about 50 nm. In the center of the gap (marked by a blue circle), the two parts of the lamella still seem to be in a minimum direct contact. A TEM analysis of the device after the full rupture (figures 5(b)–(d)) reveals a reduced gap width of less than 10 nm. The gap is visible as a fine white line in the BF-TEM image shown in figure 5(b) and amounts to approximately 8 nm in the upper part of the lamella as seen in figure 5(c), which was taken from the initial gap region. The HRTEM image reveals the stacking periodicity of the MLC stack on the left side of the gap, while only weak fringes are visible on the right side. The gap is filled with an amorphous material, most probably from hydrocarbon molecules (contamination). The absence of a gap in the HRTEM image taken from the region of the triple-phase boundary (figure 5(d)) suggests that, in that region, the two parts might still be in direct contact.

We address the difference in gap distance between the two microscopic techniques to electrostatic charging in SEM. The lower energy of the irradiating electrons results in the generation of a large number of secondary electrons, which typically cause positive charging of the insulating SiN membrane. This

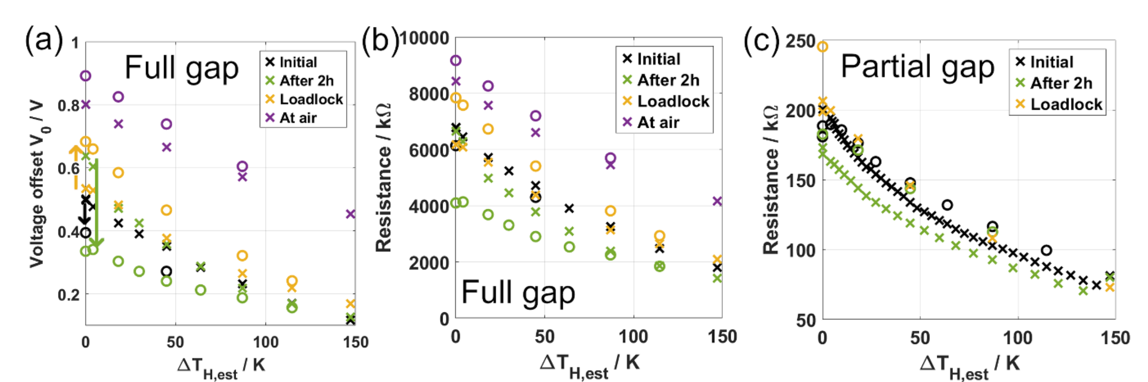

Figure 6. (a) Voltage offset plotted over the estimated temperature increase for the device with full gap and for different conditions: Directly after insertion in the microscope (blue crosses/circles), after 2 h in the microscope (red), after retraction to the loadlock (yellow) and at air (purple). Crosses represent the rise and circles the descent of the heating current. (b), (c) Measured resistances for (b) the device with full gap and (c) the device with full gap, corresponding to the voltage offsets shown in (a) and in figure 5(d), respectively.

charging, combined with the relatively poor grounding provided by conductive tape could lead to an electrostatic repulsion of the two parts of the device and thus to the large gap. In fact, this electrostatic charging could have contributed to the full rupture of the device. In contrast, electrostatic charging in TEM is negligible and the grounding given by the contact pins of the specimen holder is better, leading to the apparent closing of the gap.

Interestingly, the mechanical response of the device with full gap to an applied differential heating current I_H is highly similar when compared to the case of a partial gap. Supplementary video S5 shows the BF-TEM image evolution with increasing I_H and reveals a highly similar bending contour contrast. Figure 5(b) shows a BF-TEM image of the unheated device, acquired under similar conditions compared to figure 2(e). A comparison of both images reveals that the bending contours are slightly broader in the left part of the device for the full gap, indicating a slightly reduced initial bending of the device. The movement of the bending contours then follows a similar evolution as observed for the partial gap as seen from supplementary video S5 and the BF-TEM acquired at $I_H = 5$ mA shown in figure 5(e). The SAED pattern acquired in the unheated state (figure 5(f)) again shows the [310] crystal orientation of the material.

In contrast, a strong change is observed for the electrical properties. Figure 6(a) depicts the voltage offset determined in dependence of $\Delta T_{H,est}$, similarly as conducted for figure 4(b). The striking difference is the magnitude of the measured voltage offset, which is between 0.3 and 0.9 V, more than 30 times larger than for a partial gap. This confirms that the induced voltage offset is indeed related to the gap, as its contribution can be expected to be strongly increased in case of the full gap. Figure 6(a) shows the results for measurements conducted under different vacuum conditions. The black crosses and circles represent the first measurement after insertion into the microscope. Three additional measurements have been added: one measurement after 2 h in the microscope (green symbols), a measurement after retraction to the loadlock (yellow symbols) and at ambient pressure after full retraction from the microscope (purple symbols). The shape is similar for all of the measurements, showing a general decrease of the induced voltage offset for increasing $\Delta T_{H,est}$. A difference is seen for the rise (crosses) and descent (circles) for all measurements, the direction however changes in dependence of the vacuum environment. Both measurements conducted in the high vacuum of the microscope column (black and green symbols) show a reduced voltage offset at $\Delta T_{H,est} = 0$ K after the current ramp, as indicated by an arrow in figure 6(a). In contrast, the voltage offset increases after application of the current in poor vacuum conditions as seen from the measurements performed in the loadlock and at air. For the full gap, the voltage offset decreases more homogeneously with $\Delta T_{H,est}$ and the two regions with different slopes observed for the partial gap (figure 4(b)) are not seen. This suggests that the mechanical opening of the gap represents the major impact on the measurements of the full gap.

When comparing the two measurements conducted in high vacuum, the voltage offset agrees for a temperature increase larger than 50 K, reaching a value of 0.12 V at $\Delta T_{H,est} = 150$ K. However, a considerable difference is found in the voltage offset measured before performing the current ramp, which is 0.5 V for the initial measurement and 0.65 V for the measurement conducted after 2 h. This is in contrast to the device with partial gap, where repeated measurements after the initial ramp resulted in similar curves, which was explained by the removal of adsorbed molecules from the gap region. This difference

is attributed to the larger gap opening for the full gap. Firstly, a possible contribution could be minor mechanical changes of the device, which could lead to a decrease or increase of a possible direct contact between the left and right parts of the lamella after the application of a heating ramp. Secondly, the larger gap distance leads to a stronger exposure of the gap surfaces facilitating the adsorption of molecules from the vacuum environment even in a closed state. The molecules can therefore differ in both type and arrangement between the initial and the later measurement, leading to a change in the induced voltage offset in the unheated state. As hydrocarbon molecules are adsorbed with less adsorption energy, it is reasonable to assume that their presence and thus effect will reduce with the time of the device under high vacuum. The higher initial voltage offset after 2 h in the microscope might thus be attributed to a higher amount of water molecules. In a heated state, the impact of the gap is reduced, leading to the agreement at higher applied currents. Similar to the partial gap, the heating and opening again leads to the removal of adsorbed molecules, which explains the reduced voltage offset after the heating cycle. The measured voltage offset can again be used to estimate the electrical field strength within the gap region in the unheated state. Assuming the gap to span over the full device with a width of 8 nm, the field strength is found to be increased to 14–37 kV m^{-1}.

In addition to the voltage offset, the *I*–*V* curves also provide a value for the resistance of the device. Therefore, the curve is fitted by a linear function for lower applied voltages and the resistance is determined from the gradient. The resistances determined for both, full and partial gap are shown in dependence of $\Delta T_{\mathrm{H,est}}$ in figures 6(b) and (c), respectively. The initial resistance in the unheated state strongly increases for the full gap by more than 30 times from approximately 200 kΩ–7 MΩ. This increase is expected as the device with partial gap still possessed a large continuous connection of the material, while such a direct connection is reduced to a minimum for the full gap. When neglecting a possible contribution of the gap to the resistance value of the device with partial gap, the resistivity calculates to 0.6 Ωm, which is close to the literature value of the CCO device [15], indicating that for the device with partial gap, the resistance is governed by the material.

The measured resistance in the unheated state suggests that the partial gap only has a minor impact on the resistance, which is confirmed by the comparison of the resistance curves for the different vacuum conditions in figure 6(c). All curves show a highly similar trend towards lower resistance with increasing temperature, which can be attributed to the increase in conductivity of the semiconductive CCO material with temperature. In contrast, the measured resistance strongly differs for the different vacuum environments and current histories in case of the full gap (figure 6(b)). The differences between rise and descent are similar to the measured voltage offset. The resistance at $\Delta T_{\mathrm{H,est}} = 0$ K decreases after the current ramp in case of good vacuum conditions (black and green symbols in figure 6(b) and otherwise increases after the current ramp (yellow and purple symbols). Again, these observations could be explained by the amount of molecules present in the gap region. Under good vacuum conditions, the contribution of poorly conducting water molecules are expected to decrease after heating up, possibly leading to a better contact between the two parts of the lamella. Under worse vacuum conditions, the trend is reversed.

3.5. Summary of observed phenomena

Table 1 summarizes the different effects of the induced external stimuli due to the application of a differential heating current. The current firstly induces a temperature increase and the induction of a temperature gradient along the device. The temperature increase of approximately 150 K at maximum heating current is moderate but still increases the desorption probability of adsorbed molecules. Furthermore, it increases the conductivity of the semiconducting CCO material leading to a reduced device resistivity. In addition, a temperature gradient is generated along the device, which induces a thermovoltage within the CCO material. However, its magnitude remains small compared to the effect of the nano-gap, particularly for the full gap.

The temperature increase generates a thermal expansion of device and *in-situ* chip, which induces a mechanical bending and the opening of the gap, i.e. the exposure of interior surfaces of the gap. This opening directly diminishes the gaps' influence on the electrical measurement. In combination with a change in the vacuum environment, the gap opening leads to a modification of the density and species of adsorbed molecules within the gap. This alters the gaps' electrical contribution in both the heated and unheated state, i.e. even after gap closing. The electrical properties of the device are therefore dependent on the combined history of vacuum environment and application of differential heating currents.

Table 1. Different contributions to the observed electrical properties of the nano-accordion.

External stimulus	Effect on gap chemistry	Effect on electrical properties
Temperature increase	Increased desorption	Conductivity increase of semiconducting CCO: reduced device resistance
Temperature gradient	—	Increasing thermovoltage
Gap opening due to mechanical bending	Exposure of interior surfaces	Reduction of gap contribution
Pressure decrease/increase	Decrease/increase of adsorption, modification of gap composition	Increase/decrease of gap contribution

4. Conclusion

This work presents the nano-accordion, an *in-situ* TEM device made of a MLC material with implemented nano-gap and details its mechanical and electrical response to an applied differential heating current. The gap formed at a grain boundary and initially remained only partially spanning the device. TEM investigations for varying applied heating currents revealed a highly controllable mechanical bending of the device, which reminds the moving bellows of an accordion. The bending also induced the opening of the gap. The electrical characterizations show a high induced intrinsic voltage, which is attributed to (water) molecules adsorbed in the gap region, which are forced to desorb upon exposure of interior surfaces and heating under high vacuum conditions, leading to a reduced intrinsic voltage in the unheated state. In contrast, the initial intrinsic voltage is restored when opening the gap under worse vacuum conditions, where (water) molecules can re-adsorb. The gap expanded to spread the whole device, which only had a small impact on the mechanical response to an applied heating current, but a strong influence on the electrical properties, which were found to be dominated by the full gap. The measurements allow to calculate the electric field strength within the gap region, which amounts up to $37\,\mathrm{kV\,m^{-1}}$.

The work is of interest as it provides a way to prepare a nano-sized gap in a controlled way by specifically locating grain boundaries or pores in a material. Such electrically controlled gaps could be used to study, e.g. the electrical properties of specific gases. Moreover, this study allows drawing conclusions for the conduction of *in-situ* TEM experiments as it reveals that considerable mechanical stresses and bending can occur upon *in-situ* heating, which need to be taken into account for a correct interpretation of the acquired data.

Acknowledgments

The authors acknowledge funding from the European Union's Horizon 2020 research and innovation programme under the Marie Sklodowska-Curie Grant Agreement No 889546 and by the Spanish MICIU with funding from European Union Next Generation EU (PRTR-C17.I1) promoted by the Government of Aragon as well as from the Spanish MICIU (PID2023-151080NB-I00/AEI/10.13039/501100011033 and CEX2023-001286-S MICIU/AEI/10.13039/501100011033) and the Government of Aragon (DGA) through the Project E-13 23 R. Sample courtesy from A. Sotelo (INMA, Universidad de Zaragoza). The microscopy works have been conducted in the Laboratorio de Microscopias Avanzadas (LMA) at Universidad de Zaragoza.

Data availability statement

The data that support the findings of this study are openly available at the following URL/DOI:https://doi.org/10.5281/zenodo.17549328.[22]

Nano-accordion: Additional data available at https://doi.org/10.1088/1367-2630/ae4e52/data1.

Nano-accordion: BFTEM response available at https://doi.org/10.1088/1367-2630/ae4e52/data2.

Nano-accordion: DFTEM response available at https://doi.org/10.1088/1367-2630/ae4e52/data3.

Nano-accordion: HAADF response available at https://doi.org/10.1088/1367-2630/ae4e52/data4.

Nano-accordion: SAED response available at https://doi.org/10.1088/1367-2630/ae4e52/data5.

Nano-accordion: BFTEM full gap available at https://doi.org/10.1088/1367-2630/ae4e52/data6.

ORCID iDs

Simon Hettler 0000-0002-9102-7895
Raul Arenal 0000-0002-2071-9093

References

[1] Mayadas A F and Shatzkes M 1970 Electrical-resistivity model for polycrystalline films: the case of arbitrary reflection at external surfaces *Phys. Rev.* B **1** 1382–9
[2] Andrews P V, West M B and Robeson C R 1969 The effect of grain boundaries on the electrical resistivity of polycrystalline copper and aluminium *Phil. Mag.* **19** 887–98
[3] Fava M, Dongre B, Carrete J, van Roekeghem A, Madsen G K H and Mingo N 2021 Effects of doping substitutions on the thermal conductivity of half-Heusler compounds *Phys. Rev.* B **103** 174112
[4] Mypati O, Kumar P P, Pal S K and Srirangam P 2022 Tem analysis and molecular dynamics simulation of graphene coated AL-CU micro joints *Carbon Trends* **9** 100223
[5] Villoro R B, Wood M, Luo T, Bishara H, Abdellaoui L, Zavanelli D, Gault B, Snyder G J, Scheu C and Zhang S 2023 Fe segregation as a tool to enhance electrical conductivity of grain boundaries in Ti(Co,Fe)Sb half heusler thermoelectrics *Acta Mater.* **249** 118816
[6] Dong L, Yang F, Yu T, Zhang N, Zhou X, Xie Z and Fang F 2023 Contribution of grain boundary to strength and electrical conductivity of annealed copper wires *J. Mater. Res.Technol.* **26** 1459–68
[7] Graham R L, Alers G B, Mountsier T, Shamma N, Dhuey S, Cabrini S, Geiss R H, Read D T and Peddeti S 2010 Resistivity dominated by surface scattering in sub-50 nm Cu wires *Appl. Phys. Lett.* **96** 042116
[8] Bishara H, Lee S, Brink T, Ghidelli M and Dehm G 2021 Understanding grain boundary electrical resistivity in cu: the effect of boundary structure *ACS Nano* **15** 16607–15
[9] Aslam Z, Nicholls R, Koos A A, Nicolosi V and Grobert N 2011 Investigating the structural, electronic and chemical evolution of B-doped multi-walled carbon nanotubes as a result of joule heating *J. Phys. Chem.* C **115** 25019–22
[10] Hettler S, Sebastian D, Pelaez-Fernandez M, Benito A M, Maser W K and Arenal R 2021 In-situ reduction by joule heating and measurement of electrical conductivity of graphene oxide in a transmission electron microscope *2D Mater.* **8** 031001
[11] Hsueh Y-H, Ranjan A, Lyu L-M, Hsiao K-Y, Chang Y-C, Lu M-P and Lu M-Y 2023 In situ/operando studies for reduced eletromigration in Ag nanowires with stacking faults *Adv. Electron. Mater.* **9** 2201054
[12] Hettler S, Sreedhara M, Tenne R and Arenal R 2025 Unraveling the decomposition pathways of LaS-TaS_2 Misfit-layered compound nanostructures under extreme electrical currents by in situ TEM *J. Phys. Chem.* C **129** 13803–12
[13] Hettler S, Furqan M, Sotelo A and Arenal R 2025 Toward quantitative thermoelectric characterization of (nano) materials by in-situ transmission electron microscopy *Ultramicroscopy* **268** 114071
[14] Ng N and McQueen T M 2022 Misfit layered compounds: unique, tunable heterostructured materials with untapped properties *APL Mater.* **10** 100901
[15] Torres M A, Madre M A, Dura O J, García G, Marinel S, Martinez-Filgueira P and Sotelo A 2022 Evaluation of pressure and temperature effect on the structure and properties of $Ca_{2.93}Sr_{0.07}Co_4O_9$ ceramic materials *Ceram. Int.* **48** 7730–47
[16] Seto Y and Ohtsuka M 2022 ReciPro: free and open-source multipurpose crystallographic software integrating a crystal model database and viewer, diffraction and microscopy simulators and diffraction data analysis tools *J. Appl. Crystallogr.* **55** 397–410
[17] Miyazaki Y, Onoda M, Oku T, Kikuchi M, Ishii Y, Ono Y, Morii Y and Kajitani T 2002 Modulated structure of the thermoelectric compound $[Ca_2CoO_3]_{0.62}CoO_2$ *J. Phys. Soc. Jpn.* **71** 491–7
[18] Panchakarla L S, Lajaunie L, Ramasubramaniam A, Arenal R and Tenne R 2016 Nanotubes from oxide-based misfit family: the case of calcium cobalt oxide *ACS Nano* **10** 6248–56
[19] Heras J and Viscido L 1980 Work function changes upon water contamination of metal surfaces *Appl. Surf. Sci.* **4** 238–41
[20] Hettler S, Kano E, Dries M, Gerthsen D, Pfaffmann L, Bruns M, Beleggia M and Malac M 2018 Charging of carbon thin films in scanning and phase-plate transmission electron microscopy *Ultramicroscopy* **184** 252–66
[21] Malac M, Hettler S, Hayashida M, Kawasaki M, Konyuba Y, Okura Y, Iijima H, Ishikawa I and Beleggia M 2017 Computer simulations analysis for determining the polarity of charge generated by high energy electron irradiation of a thin film *Micron* **100** 10–22
[22] Hettler S 2025 Raw Data for the publication Mechanical and electrical properties of a nano-gap or how to play the nano-accordion *Zenodo* (https://doi.org/10.5281/zenodo.17549328)